DOI: 10.1002/ejic.200701026

A Versatile and Low-Toxicity Route for the Production of Electroceramic Oxide Nanopowders

Alejandro Morata,[a] Anthony Chesnaud,[b] Alberto Tarancón,[a] Sonia Estradé,[a] Francesca Peiró,[a] Joan-Ramon Morante,[a] and Guilhem Dezanneau*[b]

Keywords: Solid oxide fuel cells / Electrolytes / Electrodes / Nanopowders / Synthesis

An alternative route to acrylamide gel polymerisation is presented for the preparation of oxide nanopowders. Within this method, cations first dissolved in an aqueous solution are subsequently trapped inside a 3D chelating gel before fast-drying, which leads to a stable precursor. In this study, we have prepared compositions corresponding to a wide range of state-of-the-art fuel cells materials such as: $Zr_{0.85}Y_{0.15}O_{1.875}$, $Ce_{0.9}Gd_{0.1}O_{1.95}$, $Nd_{1.95}NiO_{4+x}$, $GdBaCo_2O_{5+x}$, $Ba_{0.5}Sr_{0.5}Co_{0.8}Fe_{0.2}O_{3-x}$ and $La_{0.75}Sr_{0.25}Cr_{0.5}Mn_{0.5}O_3$. Thermogravimetry and differential thermal analysis studies have been performed to determine the best calcination conditions. After calcination, the resulting powders have been characterised by X-ray diffraction, FEG-scanning electron microscopy and TEM. The synthesised powders are of nanometric crystallite size and have flake-like aggregates; pure phases are obtained at low temperature. We made this method more attractive by using a nontoxic polymer and a nonexplosive initiator. This route allows the easy preparation of more than tens of grams of nanometric powders in one batch. Finally, since this process is largely independent of the formula of the compound, it can easily be extended to other kinds of oxides such as ferroelectric, CMR (colossal magnetoresistance) or gas sensor compounds.

Introduction

The harsh working conditions of solid state devices in the field of fuel cells have stirred the research on new ceramic materials with controlled characteristics.[1] Although conventional solid state synthesis methods have the advantage of high simplicity, they require high temperatures and very long annealing times that entail excessive crystal growth. Many efforts have thus been devoted to the development of low-cost reproducible synthesis routes that can easily be transferred to the industrial scale. Wet chemistry routes such as the sol–gel and Pechini methods have given interesting results, as the ion mixing occurs at a molecular scale. Sol–gel chemistry is a remarkably versatile approach for the fabrication of ceramic powders at low temperatures.[2] Nevertheless, in most of cases, the application of a sol–gel route involves a high complexity due to the necessity of a fine adjustment of parameters.[3] The Pechini method is more versatile, because the technique has a strong robustness and requires less or null adaptation from one material to the other. Several works have also presented the application of the glycine nitrate combustion route for the preparation of complex electrolyte oxides.[4–6] This last process leads to interesting results, presenting a lower complexity relative to the sol–gel or Pechini methods. Nevertheless, it seems to be difficult to obtain the desired phase, and strong aggregates appear as a result of the coarsening of the powders during the burning step.[6] Moreover, a minimum annealing temperature of 800 °C is needed to remove all residual organic components,[4] which entail a limitation for the synthesis of many materials. Additionally, the ratio of the departing organic products needs to be tuned for the synthesis of different materials, involving a hindrance for a straightforward extensive application. Finally, another well-known technique that leads to good results is the so-called freeze-drying process.[7] This route has proven to be efficient and industrially scalable. Nevertheless, the procedure is time-consuming and needs a sophisticated setup.

An alternative method, the so-called acrylamide route, was proposed for the synthesis of functional oxides.[8] This method has recently been applied to a broad range of electroceramic oxides for fuel cells.[9–11] It consists of the trapping of dissolved cations in an acrylamide polymer network. In this manner, an intimate mixing is performed at the molecular level, and the chelating properties of the polymer allow maintaining cations separated during the drying of the gel. One of the main drawbacks of acrylamide gel combustion lays in the toxicity of the acrylamide monomer and the hazardous properties of the azoisobutyronitrile initiator. In a previous article, we showed that the substitution of acrylamide by methacrylamide, which has limited toxic-

[a] Electronics Department, University of Barcelona, C/Martí i Franquès, Barcelona 08028, Spain
[b] Laboratoire Structures, Propriétés et Modélisation des Solides, Ecole Centrale Paris, Grande voie des vignes, 92295 Châtenay-Malabry, France
E-mail: guilhem.dezanneau@ecp.fr

ity, was possible without modification of the process.[9] Nevertheless, the use of methacrylamide leads to much weaker gels, and the oxide nanopowders look more agglomerated. Since the main interest for acrylamide in the process resides in its facility to polymerise in a wide range of pH values and in its chelating properties, this led us to naturally consider the possibility of using a much more common monomer, acrylic acid, also known for its chelating properties.

In order to overcome the problem of acrylamide toxicity, the use of acrylic acid as an alternative was thus studied here. We also demonstrate that the use of azoisobutyronitrile (AIBN) as initiator is not necessary and AIBN can easily be substituted by the cheaper and less dangerous hydrogen peroxide, H_2O_2. We present here, as an illustration of the wide possibilities of such a method, the synthesis of several oxide materials constituting the state-of-the-art in the SOFC (solid oxide fuel cell) domain. The structural and microstructural properties of these materials have been characterised and related to the elements constituting the process.

Results and Discussion

Calcination Step

Under the preparation conditions described below and regardless of composition, the gel obtained after polymerisation looks like the one presented in Figure 1. After drying this gel in a microwave oven, the decomposition process of the precursor, a brown crisp resin, was recorded by means of TG-DTA. As shown in Figure 2a and 2b, the TGA and DTA curves for the calcination of the precursor are almost similar regardless of composition. The TG curves show that decomposition, which is associated with an important weight loss ($\Delta m \approx 80\%$), occurs in two or three steps between room temp. and 450 °C. Nevertheless, the most important weight loss, which was observed between 300 °C and 400 °C, occurred during the second step of the decomposition process. DTA (see Figure 2b) reveals this effect by the presence of two or three exothermic peaks in this temperature range. From 300 °C, it is clear that the exothermicity is strongly correlated to the nitrate content in the dried precursor. Indeed, while synthesis conditions are identical, the amount of nitrate introduced into one solution is not the same from one sample to the other. Besides, the topology and hardness of the gel are controlled by the monomer/reticulant ratio. Indeed, a more reticulating gel could be obtained decreasing the amount of monomer. Thus, if acrylic acid is also implied in cation complexation, the topology of the gel might be slightly different and its ignition temperature will also be different. The first decomposition at ca. 200 °C, involving around 15% of the total weight loss and revealed by a very weak exothermic peak on DTA curves, was probably the result of the evacuation of residual water. The two more intense peaks at temperatures ranging between 300 °C and 450 °C, leading to the remaining 85% of the lost weight, involve a two-stage decomposition mechanism. The first stage corresponds to the decomposition of the carboxylate or acrylate groups/uncomplexed ligands as already observed by using thermogravimetry coupled to mass spectrometry. The second stage of the decomposition, representing most of the weight loss, may correspond to combustion of the polymer.[12] Except for zirconia, for which a small weight loss is observed over 600 °C, all the dried precursors seem to burn the major part of the organic components below 500 °C. However, a better understanding of the gel decomposition processes would involve a GC–MS study. Above 450 °C, it can be assumed that all organic species were decomposed. While TG curves showed a plateau which extends up to 1000 °C, no DTA signals were recorded. This may also indicate that crystallisation of products already occurs during one of the exothermic steps mentioned above. Actually, all the products show

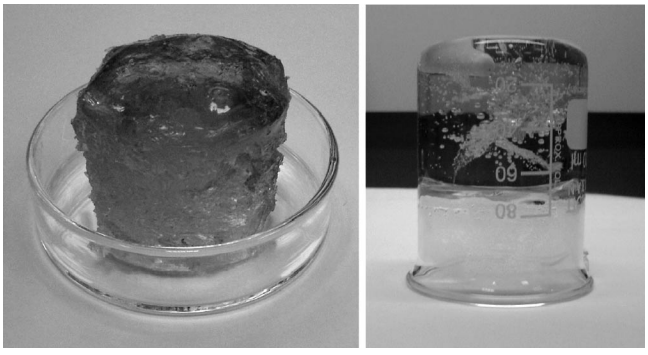

Figure 1. Typical appearance of the polymerised gels.

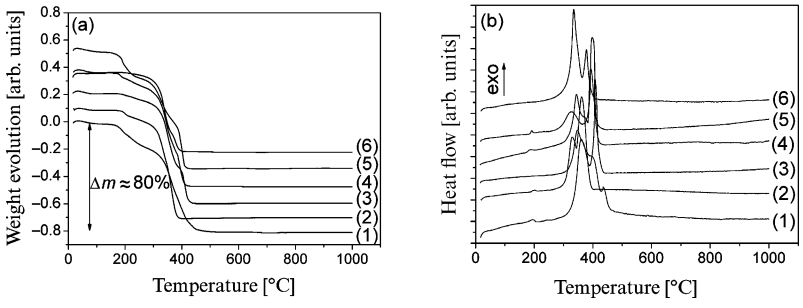

Figure 2. TG and DTA curves of samples (1) $Zr_{0.85}Y_{0.15}O_{1.875}$, (2) $Ce_{0.9}Gd_{0.1}O_{1.95}$, (3) $Nd_{1.95}NiO_{4+x}$, (4) $GdBaCo_2O_{5+x}$, (5) $Ba_{0.5}Sr_{0.5}Co_{0.8}Fe_{0.2}O_{4-d}$, (6) $La_{0.75}Sr_{0.25}Cr_{0.5}Mn_{0.5}O_3$: microwave drying as a function of temperature.

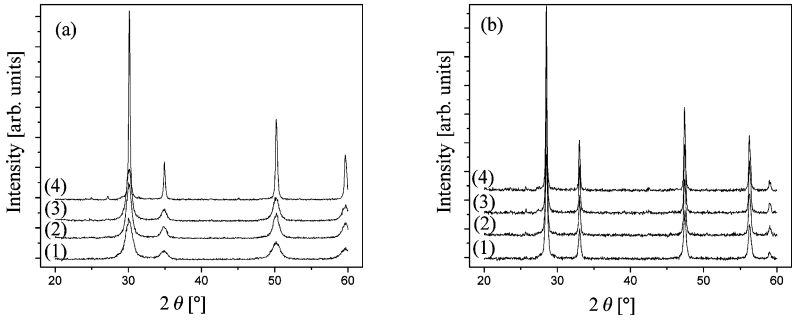

Figure 3. X-ray diffraction patterns of (a) $Zr_{0.85}Y_{0.15}O_{1.875}$ and (b) $Ce_{0.9}Gd_{0.1}O_{1.95}$ electrolyte materials annealed for 4 h at (1) 700 °C, (2) 800 °C, (3) 900 °C and (4) 1000 °C.

crystalline phases after calcination (even after heat-treatment at 500 °C, not presented here). Nevertheless, the speed of heating used for the calcination of the powders was significantly slower (5 °C min^{-1}), which may explain the poor crystallisation level after the heat-treatment (see below).

Electrolyte Materials: $Zr_{0.85}Y_{0.15}O_{1.875}$ and $Ce_{0.9}Gd_{0.1}O_{1.95}$

The XRD diagrams corresponding to the electrolyte materials $Zr_{0.85}Y_{0.15}O_{1.875}$ and $Ce_{0.9}Gd_{0.1}O_{1.95}$ are shown in Figure 3. In both cases, the pure phase is obtained at a very low temperature, showing very broad peaks. This is an indication of the very small size of the crystallites composing the powder. The average values of the grain sizes of the synthesised powders, obtained by using the well known Scherrer formula, are 9(1) nm for zirconia and 28(1) nm for ceria in the case of samples heat-treated at 700 °C for 4 h. This difference was also demonstrated in our previous work based on the acrylamide polymerisation synthesis route[9] and has been previously reported by other authors.[13] The reason for this behaviour may be the better sinterability of cerium-based fluorite oxides as compared to the zirconium-based ones. Actually, Li et al.[14] reported that 99% density cerium oxide ceramics can be obtained at a temperature as low as 1160 °C, while zirconia-based ceramics are usually fully densified at temperatures of at least 1300–1400 °C.[15]

The observation by scanning electron microscopy (SEM) reveals that the powders present sheet-like aggregates of several microns with nanometric grain sizes as foreseen by XRD (Figure 4). Nevertheless, the native grain sizes can hardly be seen with this technique. The observation by TEM shown in Figure 5 confirms the nanometric nature of the grains and also the great differences in terms of grain sizes between the two powders. The calculation of grain sizes as determined by TEM pictures leads to a mean grain size of 6.5(2.0) nm for zirconia and 22(2) nm for ceria, values that are close to the ones obtained from XRD.

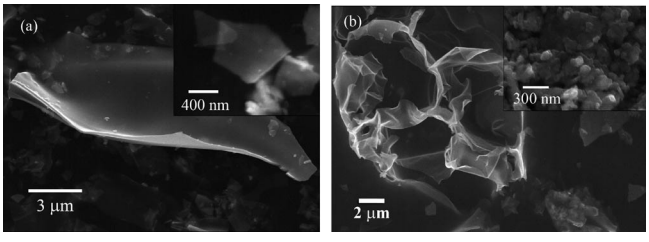

Figure 4. FEG-SEM images of (a) $Zr_{0.85}Y_{0.15}O_{1.875}$ and (b) $Ce_{0.9}Gd_{0.1}O_{1.95}$ annealed at 700 °C for 4 h.

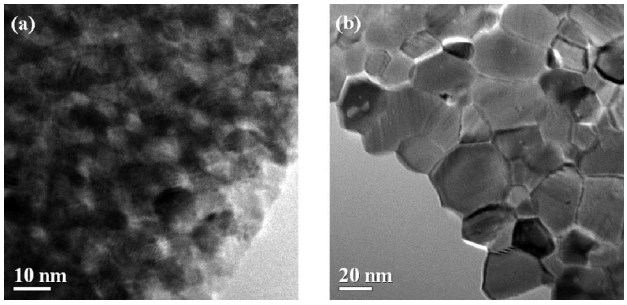

Figure 5. TEM images of (a) $Zr_{0.85}Y_{0.15}O_{1.875}$ and (b) $Ce_{0.9}Gd_{0.1}O_{1.95}$ annealed at 700 °C for 4 h.

Cathode Materials: $Nd_{1.95}NiO_{4+x}$, $GdBaCo_2O_{5+x}$, $Ba_{0.5}Sr_{0.5}Co_{0.8}Fe_{0.2}O_{3-x}$

The diffractograms in Figure 6 give the evolution of crystal structures with temperature for the samples corresponding to electrode materials. All the desired phases are formed below 1000 °C. For the $Nd_{1.95}NiO_{4+x}$, the XRD diagrams obtained on samples heat-treated at low temperature, 700 °C and 800 °C, reveal the presence of the perovskite phase $NdNiO_3$ [Joint Committee for Powder Diffraction Society (JCPDS), pattern no. 41-0344] and of the simple oxide Nd_2O_3 (JCPDS pattern no. 43-1023). The desired phase is readily formed at 900 °C, and no parasitic phase is observed. Similarly, for the $GdBaCo_2O_{5+x}$ sample heat-treated at 700 °C and 800 °C, the X-ray diffraction diagrams are composed of very wide peaks that can be attributed to $BaCoO_{2.93}$ (JCPDS pattern no. 26-0144) and $GdCoO_3$ (JCPDS pattern no. 25-1057), both being perovskite-like phases. Here also, a calcination temperature of 900 °C is necessary to obtain the pure phase. In the case of $Ba_{0.5}Sr_{0.5}Co_{0.8}Fe_{0.2}O_{3-x}$, a pure phase is also observed from 900 °C onwards. Grain sizes have been determined from the

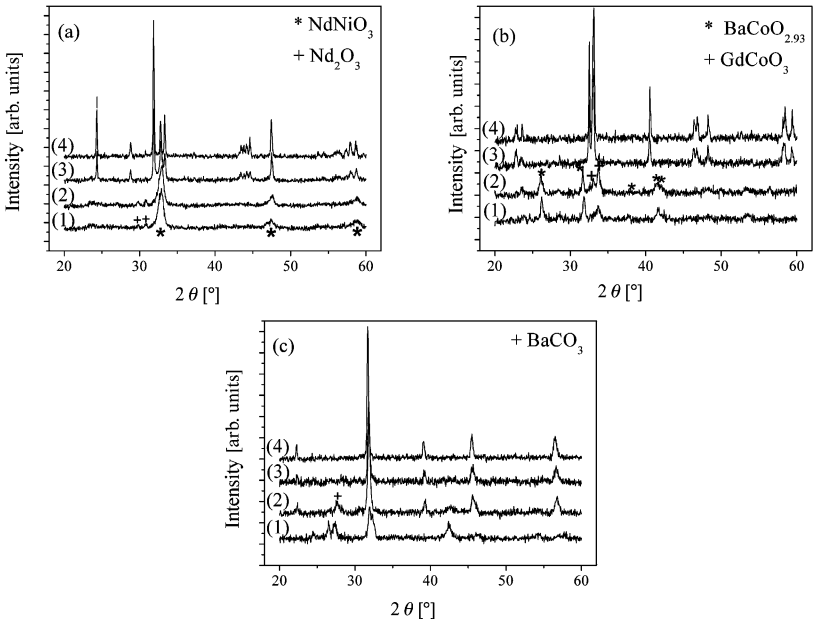

Figure 6. X-ray diffraction patterns of (a) $Nd_{1.95}NiO_{4+x}$, (b) $GdBaCo_2O_{5+x}$, (c) $Ba_{0.5}Sr_{0.5}Co_{0.8}Fe_{0.2}O_{3-x}$, annealed for 4 h at (1) 700 °C, (2) 800 °C, (3) 900 °C and (4) 1000 °C.

Scherrer laws applied on single peaks in pure-phase compounds. From this law, we calculated that the grain sizes of the cathode materials heat-treated at 900 °C are 60(1) nm for $Nd_{1.95}NiO_{4+x}$ (Figure 6a), 58(1) nm for $GdBaCo_2O_{5+x}$ (Figure 6b) and 35(1) nm for $Ba_{0.5}Sr_{0.5}Co_{0.8}Fe_{0.2}O_{3-x}$ (Figure 6c).

In Figure 7, representative SEM-FEG images show the microstructure of these cathode materials obtained at 900 °C. The powders consist of very porous aggregates of nanometric weakly connected crystallites. The $Ba_{0.5}Sr_{0.5}Co_{0.8}Fe_{0.2}O_{3-x}$ particles are the more strongly bonded ones (Figure 6c). They seem to be connected to form grains of about 500 nm, which in turn constitute micrometric porous planar flake-like microstructures. This can be due to the fact that this material already presents the perovskite phase at low temperatures. The excessive temperature necessary to eliminate barium carbonate may be responsible for the partial sintering of the small particles. From these SEM images, it seems that native grains have bigger sizes than the ones given by XRD. Nevertheless, TEM observations in Figure 8 confirm that the differences in the grain sizes between the different compositions follow the order $\Phi(Nd_{1.95}NiO_{4+x}) > \Phi(GdBaCo_2O_{5+x}) > \Phi(Ba_{0.5}Sr_{0.5}Co_{0.8}Fe_{0.2}O_{3-x})$ as deduced from XRD. Besides, it seems in this picture that $Nd_{1.95}NiO_{4+x}$ presents a nonhomogeneous distribution of grain sizes (Figure 8a).

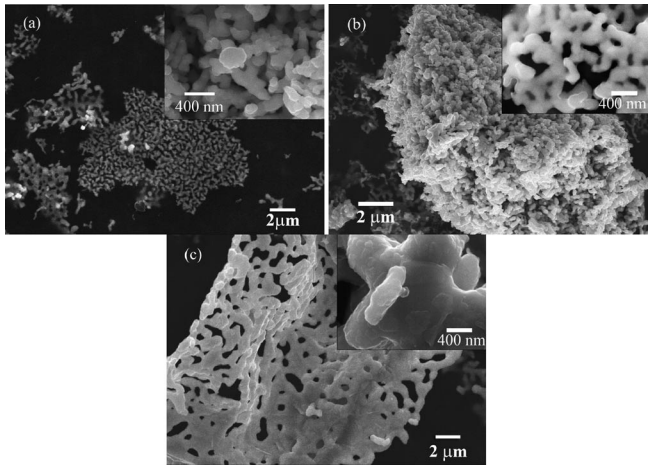

Figure 7. SEM-FEG images of (a) $Nd_{1.95}NiO_{4+x}$, (b) $GdBaCo_2O_{5+x}$ and (c) $Ba_{0.5}Sr_{0.5}Co_{0.8}Fe_{0.2}O_{3-x}$ annealed at 900 °C.

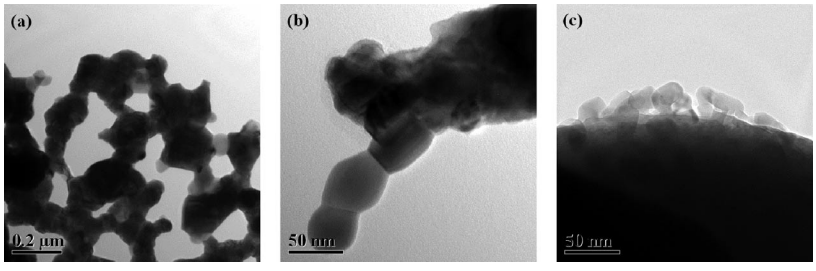

Figure 8. TEM images of (a) $Nd_{1.95}NiO_{4+x}$, (b) $GdBaCo_2O_{5+x}$ and (c) $Ba_{0.5}Sr_{0.5}Co_{0.8}Fe_{0.2}O_{3-x}$ annealed at 900 °C.

Anode Material: $La_{0.75}Sr_{0.25}Cr_{0.5}Mn_{0.5}O_3$

The phase evolution of the $La_{0.75}Sr_{0.25}Cr_{0.5}Mn_{0.5}O_3$ precursor with the calcination temperature is shown in Figure 9 by means of XRD measurements at 700 °C, 800 °C, 900 °C and 1000 °C. The desired phase is already formed at 700 °C. Nevertheless, very small diffraction peaks corresponding to the $SrCrO_4$ phase are still observed (JCPDS pattern no. 35-0743). These small peaks progressively disappear with increasing temperature. All the peaks observed at 1000 °C can be attributed to the desired perovskite phase. Nevertheless, the diffractogram shows some splitting of the main perovskite peaks, revealing a certain degree of distortion of the cubic structure (that is the expected structure). In particular, the main peak at 32° seems to be composed of at least three contributions. The mean crystallite size as obtained from the single peak (at 22°), is 30 nm. Electron microscopy images illustrate the morphology of the synthesised powder (Figure 10). The powder consists of nanometric connected crystallites forming very porous sponge-like structures. The grain size as deduced from TEM pictures is 21(4) nm, which is also rather close to the value determined form XRD.

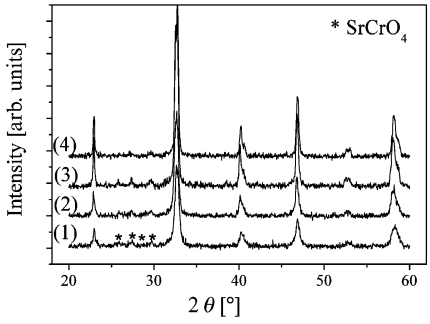

Figure 9. X-ray diffraction patterns of $La_{0.75}Sr_{0.25}Cr_{0.5}Mn_{0.5}O_3$ annealed for 4 h at (1) 700 °C, (2) 800 °C, (3) 900 °C and (4) 1000 °C.

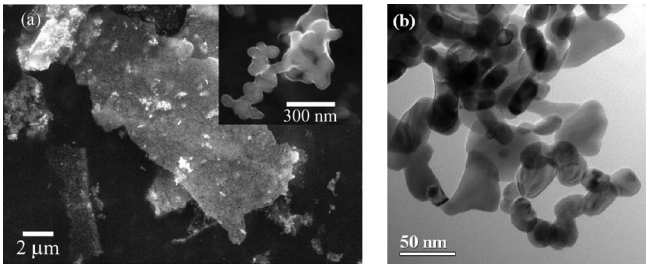

Figure 10. (a) SEM and (b) TEM images of the $La_{0.75}Sr_{0.25}Cr_{0.5}Mn_{0.5}O_3$ sample heat-treated at 900 °C for 4 h.

Discussion

The necessity to replace acrylamide for safety reasons in the acrylamide gel combustion route led us to find another monomer presenting similar properties. Acrylic acid has been chosen for different reasons. Its low toxicity is the first parameter that we took into account, since this is one of the main drawbacks of acrylamide. As a result of its non-toxicity, the acrylic acid monomer is widely employed in dental and orthopaedic products. Secondly, acrylic acid based polymers are well-known for their excellent water-absorbing properties. This is of great importance here in avoiding solution–polymer phase separation when the polymerisation occurs.[16] Moreover, polyacrylic acid polymers present interesting complexation properties. Actually, several studies show that this complexation behaviour is effectively seen in a wide diversity of elements such as transition-metal cations, alkaline-earth elements or rare-earth elements.[12,17–19] Besides, the complexation power of acrylic acid depends strongly on pH,[12] the optimum pH being around 5–6, which is very close to the pH value used in the present study. These studies also showed that the decomposition of acrylic acid complex is complete between 400–550 °C and depends on the cations present because some of them have catalytic power (Cu^{2+} for instance). In our case, we observe a similar range of temperatures for the decomposition of our precursor, and the highest decomposition rate always occurs at almost the same temperature (≈ 400 °C) regardless of composition. This means that the grain size distribution and agglomeration of the resulting powder will essentially depend on the sinterability of the material.

Of course, because of the addition of citric acid during the process, one may think that the method is similar to the citrate gel route. Actually, the main similarity is that, in both routes, the chelating properties of the species used (citric acid or acrylic acid) prevent the precipitation of cation salts. Nevertheless, we think that the presented method has some significant advantages over the citrate gel route. One of them is that the polymerisation occurs very fast (in less than 5 min), while according to literature, the citrate gel route implies a slow polymerisation accompanied by evaporation of solvent (water). This slow evaporation is time-consuming. Actually, some treatments that take as long as 10 h have been reported for obtaining a viscous gel,[21–22] but more typically the gelling time is around 2–3 h.[23] Another consequence of this slow evaporation is that species are put closer; so the next step involving the combustion process may lead to more aggregated particles. In our case, the combustion process occurs partly during the microwave drying, which leads to a precursor with a brownish colour. Then, the microstructure of our oxide nanopowders after calcination is typical of processes for which a great quantity of organic species is burnt very fast. In these cases, it is often argued that the great amount of gaseous species that are produced during heat-treatment leads to more aeration, resulting in powders with soft aggregates and sheet-like morphology. This microstructure may have some important advantages for the SOFC applications. First, the nanometric nature of oxide powders favour the control of sintering process and may lead to higher density at low temperature. The obtained nanopowders may also be interesting for electrode applications, since both gas diffusion and electrical percolation should be favoured by this peculiar morphology. Let us note finally that, in the case of electrode materials, the synthesis temperature of 900 °C is lower than or compar-

able to those mentioned in previous articles. For instance, Lalanne et al. mention that a temperature of 1000 °C is necessary to obtain pure $Nd_{1.95}NiO_{4+x}$ by either the citrate gel or the acrylamide polymerisation methods.[24] $Ba_{0.5}Sr_{0.5}Co_{0.8}Fe_{0.2}O_{3-x}$ has been the subject of much research because of its potential use in semipermeable membrane applications. This compound can be obtained at a rather low temperature between 850 °C and 1000 °C, temperatures comparable to the one (900 °C) needed in this study to obtain the pure phase.[25–27] There are not many studies on $GdBaCo_2O_{5+x}$, because the use of this material for fuel cell applications is quite recent. Nevertheless, synthesis temperatures of 1125 °C[35] and 1000 °C[36] have been mentioned, which are significantly higher than 900 °C. Finally, for LSCM, heat-treatment temperatures of 1300 °C,[28] 1200 °C,[29] 1100 °C[30] or 800 °C[31] are reported for the preparation of a pure phase; most of them are still higher than 900 °C.

Conclusions

In the present article, we have shown that a good alternative to the use of highly toxic acrylamide in the complexing gel combustion route can be the use of acrylic acid. The method is very fast, since less than one hour is necessary to obtain an easy-to-handle precursor. It is also efficient, since single-phase compounds are obtained at low temperature. We have also shown that the method is very versatile, as no modification is necessary when changing the composition. The resulting powders are nanometric and present a flake-like microstructure. In all compositions presented here, single-phase compounds are obtained at temperatures as low as 900 °C. The method is then promising for applications in SOFCs but can also be extended to all functional oxides.

Experimental Section

For the present study, the different materials studied have the following compositions: $Zr_{0.85}Y_{0.15}O_{1.925}$, $Ce_{0.9}Gd_{0.1}O_{1.95}$ corresponding to anion conducting electrolyte materials, $Ba_5Sr_{0.5}Co_{0.8}Fe_{0.2}O_{3-x}$, $GdBaCo_2O_{5+x}$, $Nd_{1.95}NiO_{4+x}$, used as cathodes in SOFCs and $La_{0.75}Sr_{0.25}Cr_{0.5}Mn_{0.5}O_3$ as an example of an anode material.[32–38] The cation salts used for the synthesis were the following: $Y(NO_3)_3{\cdot}6H_2O$ (Sigma–Aldrich, 99.9%), $ZrO(NO_3)_2{\cdot}xH_2O$ (Sigma–Aldrich, ≈ 27% weight in Zr), $Ce(NO_3)_3{\cdot}6H_2O$ (Sigma–Aldrich, 99%), $Gd(NO_3)_3{\cdot}xH_2O$ (Alfa-Aesar, 99.9%), $Ba(NO_3)_2$ (Alfa-Aesar, 99%), $Sr(NO_3)_2$ (Sigma–Aldrich, 99%), $La(NO_3)_3{\cdot}6H_2O$ (Sigma–Aldrich, 99.0%), $Fe(NO_3)_3{\cdot}9H_2O$ (Merck, 99%), $Co(NO_3)_3{\cdot}6H_2O$ (Merck, 99%), $Ni(NO_3)_2{\cdot}6H_2O$ (Sigma–Aldrich, 98.5%), $Mn(NO_3)_2{\cdot}6H_2O$ (Sigma–Aldrich, 98%) and $Cr(NO_3)_3{\cdot}9H_2O$ (Aldrich, 98%). The water content of precursors, in particular those of $ZrO(NO_3)_2{\cdot}xH_2O$ and $Gd(NO_3)_3{\cdot}xH_2O$, was determined by weighing the resulting mass of oxide obtained from the calcination of a known amount of precursor at 900 °C for 8 h. The organic species used were citric acid (Aldrich, 99%), acrylic acid (Aldrich, anhydrous, 99%), *N*,*N*′-methylene bis(acrylamide) (Aldrich, 99%) and hydrogen peroxide (Aldrich, 30% w/w in water). The synthesis process is as follows: Cation precursors are dissolved separately in deionised water (80–100 mL) in the proportion corresponding to the final product. The quantity of precursor is chosen in such a way that, after mixing the different cation solutions, the total cation concentration is 0.1 mol L^{-1}. For instance, in the case of yttria-stabilised zirconia, the molar quantity of precursors for 500 mL of solution is 0.0425 mol and 0.0075 mol for zirconium and yttrium, respectively. Then, citric acid is added to each cation solution in the proportion corresponding to one citric acid molecule per cation valence in solution and the pH is increased to 6 by adding ammonium hydroxide solution. The solutions are then mixed together. After heating up to 90–100 °C, acrylic acid (AA) and *N*,*N*′-methylene bis(acrylamide) (*N*,*N*′-MBA) are added, as monomer and reticulating agent, respectively. For each 500-mL solution, acrylic acid (50 mL) and MBA (2.8 mg) are used, which corresponds to an AA/MBA molar ratio equal to 40. Then, a few droplets of H_2O_2, which acts as an initiator and produces instantaneous gelification, are added to the boiling solution. The gel obtained is solid and transparent (see Figure 1). This gel is then dried in a conventional microwave oven for 30 min to obtain an easy-to-handle and stable precursor. After this drying step in the microwave oven, the precursor has a brownish colour, which shows that some combustion has already occurred during this step. It is also important to note here that this precursor has become inflated during microwave drying and occupies a volume that is even larger than the initial gel. Finally, an annealing process is performed in order to eliminate the remaining organic species and to obtain the desired phase. Different annealing temperatures were tested between 700 °C and 1000 °C.

The resulting powders were analysed with a Siemens D5000 diffractometer operating in a Bragg–Brentano geometry with a Cu-$K_{\alpha 1,2}$ wavelength. Thermogravimetry and differential thermal analysis were used to follow the elimination process of organics from the green dried product and the formation of the crystalline ceramic phases. TG and TDA have been carried out with a SETARAM TG/DSC instrument (the alumina crucible was used as reference) Model 92-1750. These analyses were undertaken in a flowing synthetic air atmosphere, from room temp. to 1000 °C, with a heating rate of 10 °C min^{-1}. SEM was performed with a Philips XL 30 apparatus equipped with a Field-Emission Gun, in order to observe the morphology of the heat-treated powders and to get information on grain sizes. TEM has also been used to get further inside the microstructure at a nanometric scale and was thus complementary to SEM characterisation for some samples with smaller grain sizes. The TEM images were obtained with a Philips CM 30 instrument at 300 kV, except for those at higher resolution obtained with a Jeol J2010F FEG instrument at 200 kV.

[1] A. Lashtabeg, S. J. Skinner, *J. Mater. Chem.* **2006**, *16*, 3161–3170.
[2] E. P. Turevskaya, M. I. Yanovskaya, N. Y. Turova, *Inorg. Mater.* **2000**, *36*, 260–270.
[3] N. Kim, B.-H. Kim, D. Lee, *J. Power Sources* **2000**, *90*, 139–143.
[4] L. Cong, T. He, Y. Ji, P. Guan, Y. Huang, W.-i. Su, *J. Alloys Compd.* **2003**, *348*, 325–331.
[5] M. Shi, N. Liu, Y. Xu, Y. Yuan, P. Majewski, F. Aldinger, *J. Alloys Compd.* **2006**, *425*, 348–352.
[6] Y. Zhai, C. Ye, F. Xia, J. Xiao, L. Dai, Y. Yang, Y. Wang, *J. Power Sources* **2006**, *162*, 146–150.
[7] T. Yokota, Y. Kubota, Y. Takahata, T. Katsuyama, Y. Matsuda, *J. Chem. Eng. Jpn.* **2004**, *37*, 238–242.
[8] A. Sin, P. Odier, *Adv. Mater.* **2000**, *12*, 649–652.
[9] A. Tarancón, G. Dezanneau, J. Arbiol, F. Peiró, J. R. Morante, *J. Power Sources* **2003**, *118*, 256–264.
[10] N. Liu, Y. Yuan, P. Majewski, F. Aldinger, *Mater. Res. Bull.* **2006**, *41*, 461–468.

[11] H. Zhang, X. Fu, S. Niu, G. Sun, Q. Xin, *J. Solid State Chem.* **2004**, *177*, 2649–2654.
[12] N. Sebastian, B. George, B. Mathew, *Polym. Degrad. Stab.* **1998**, *30*, 371–375.
[13] I. Kosacki, T. Suzuki, V. Petrovsky, H. U. Anderson, *Solid State Ionics* **2000**, *136–137*, 1225–1233.
[14] J. G. Li, T. Ikegami, J. H. Lee, T. Mori, *Acta Mater.* **2001**, *49*, 419–426.
[15] O. C. Standard, C. C. Sorell, *Key Eng. Mater.* **1998**, *153–154*, 251.
[16] M. P. Raju, K. M. Raju, *J. Appl. Polym. Sci.* **2001**, *80*, 2635–2639.
[17] H. Pesonen, A. Sillanpää, R. Aksela, K. Laasonen, *Polymer* **2005**, *46*, 12641–12652.
[18] R. Roma-Luciow, L. Sarraf, M. Morcellet, *Eur. Polym. J.* **2001**, *37*, 1741–1745.
[19] R. Roma, M. Morcellet, L. Sarraf, *Mater. Lett.* **2005**, *59*, 889–893.
[20] S. Dubinsky, G. S. Grader, G. E. Shter, M. S. Silverstein, *Polym. Degrad. Stab.* **2004**, *86*, 171–178.
[21] X. Shen, J. Zhou, M. Jing, Y. Shen, *J. of Wuhan University of Technology-Mater.* **2007**, *June*, 179.
[22] J. Bi, L. Wu, Z. Li, X. Wang, X. Fu, *Materials Letters* **2007**, in press.
[23] L. Bocher, M. H. Aguirre, R. Robert, M. Trottmann, D. Logvinovich, P. Hug, A. Weidenkaff, *Thermochim. Acta* **2007**, *457*, 11–19.
[24] C. Lalanne, F. Mauvy, E. Siebert, M. L. Fontaine, J. M. Bassat, F. Ansart, P. Stevens, J. C. Grenier, *J. Eur. Ceram. Soc.* **2007**, *27*, 4195–4198.
[25] S. Lee, Y. Lim, E. A. Lee, H. J. Hwang, J.-W. Moon, *J. Power Sources* **2006**, *157*, 848–854.
[26] A. Yan, M. Cheng, Y. Dong, W. Yang, V. Maragou, S. Song, P. Tsiakaras, *Appl. Catal. B* **2006**, *66*, 64–71.
[27] Y. Wang, S. Wang, T. Wen, Z. Wen, *J. Alloys Compd.* **2007**, *428*, 286–289.
[28] J. Wan, J. H. Zhu, J. B. Goodenough, *Solid State Ionics* **2006**, *177*, 1211–1217.
[29] Bo Huang, S. R. Wang, R. Z. Liu, X. F. Ye, H. W. Nie, X. F. Sun, T. L. Wen, *J. Power Sources* **2007**, *167*, 39–46.
[30] J. Peña-Martínez, D. Marrero-López, J. C. Ruiz-Morales, B. E. Buergler, P. Núñez, L. J. Gauckler, *J. Power Sources* **2006**, *159*, 914–921.
[31] X. J. Chen, Q. L. Liu, S. H. Chan, N. P. Brandon, K. A. Khor, *Electrochem. Commun.* **2007**, *9*, 767–772.
[32] N. P. Brandon, S. Skinner, B. C. H. Steele, *Ann. Rev. Mater. Res.* **2003**, *33*, 183–213.
[33] F. Mauvy, C. Lalanne, J. M. Bassat, J. C. Grenier, H. H. Zhao, L. H. Huo, P. Stevens, *J. Electrochem. Soc.* **2006**, *153*, A1547–A1553.
[34] E. Boehm, J. M. Bassat, P. Dordor, F. Mauvy, J. C. Grenier, P. Stevens, *Solid State Ionics* **2005**, *176*, 2717–2725.
[35] A. Chang, S. J. Skinner, J. A. Kilner, *Solid State Ionics* **2006**, *177*, 2009–2011.
[36] A. Tarancón, A. Morata, G. Dezanneau, S. J. Skinner, J. A. Kilner, S. Estradé, F. Hernández-Ramírez, F. Peiró, J. R. Morante, *J. Power Sources* **2007**, *174*, 255–263.
[37] Z. P. Shao, S. M. Haile, *Nature* **2004**, *431*, 170–173.
[38] A. Atkinson, S. Barnett, R. J. Gorte, J. T. S. Irvine, A. J. McEvoy, M. Mogensen, S. C. Singhal, J. Vohs, *Nat. Mater.* **2004**, *3*, 17–27.

Received: September 21, 2007
Published Online: January 8, 2008

